



HAL
open science

Scale-Dependent Air-Sea Exchange in the Polar Oceans: Floe-Floe and Floe-Flow Coupling in the Generation of Ice-Ocean Boundary Layer Turbulence

Samuel Brenner, Christopher Horvat, Paul Hall, Anna Lo Piccolo, Baylor
Fox-Kemper, Stéphane Labbé, Véronique Dansereau

► **To cite this version:**

Samuel Brenner, Christopher Horvat, Paul Hall, Anna Lo Piccolo, Baylor Fox-Kemper, et al..
Scale-Dependent Air-Sea Exchange in the Polar Oceans: Floe-Floe and Floe-Flow Coupling in the
Generation of Ice-Ocean Boundary Layer Turbulence. *Geophysical Research Letters*, 2023, 50,
10.1029/2023GL105703 . insu-04604353

HAL Id: insu-04604353

<https://insu.hal.science/insu-04604353>

Submitted on 7 Jun 2024

HAL is a multi-disciplinary open access archive for the deposit and dissemination of scientific research documents, whether they are published or not. The documents may come from teaching and research institutions in France or abroad, or from public or private research centers.

L'archive ouverte pluridisciplinaire **HAL**, est destinée au dépôt et à la diffusion de documents scientifiques de niveau recherche, publiés ou non, émanant des établissements d'enseignement et de recherche français ou étrangers, des laboratoires publics ou privés.



Distributed under a Creative Commons Attribution - NonCommercial 4.0 International License

Geophysical Research Letters[®]



RESEARCH LETTER

10.1029/2023GL105703

Key Points:

- Discrete element model results show floe-size-dependent ice-ocean boundary layer (IOBL) stress-driven turbulence
- IOBL turbulence is driven both by floe collisional velocity and by floe-scale ocean variability
- We present a framework for a scale-aware parameterization of IOBL turbulence using bulk parameters

Correspondence to:

S. Brenner,
sdbrenner@brown.edu

Citation:

Brenner, S., Horvat, C., Hall, P., Lo Piccolo, A., Fox-Kemper, B., Labbé, S., & Dansereau, V. (2023). Scale-dependent air-sea exchange in the polar oceans: Floe-floe and floe-flow coupling in the generation of ice-ocean boundary layer turbulence. *Geophysical Research Letters*, 50, e2023GL105703. <https://doi.org/10.1029/2023GL105703>

Received 31 JUL 2023
Accepted 18 NOV 2023

Scale-Dependent Air-Sea Exchange in the Polar Oceans: Floe-Floe and Floe-Flow Coupling in the Generation of Ice-Ocean Boundary Layer Turbulence

Samuel Brenner¹ , Christopher Horvat^{1,2} , Paul Hall¹, Anna Lo Piccolo¹, Baylor Fox-Kemper¹ , Stéphane Labbé³ , and Véronique Dansereau⁴ 

¹Brown University, Providence, RI, USA, ²The University of Auckland, Auckland, New Zealand, ³Sorbonne Université, Paris, France, ⁴Institut des Sciences de la Terre, Université Grenoble Alpes, CNRS (UMR5275), Gières, FR

Abstract Sea ice is a heterogeneous, evolving mosaic of individual floes, varying in spatial scales from meters to tens of kilometers. Both the internal dynamics of the floe mosaic (floe-floe interactions), and the evolution of floes under ocean and atmospheric forcing (floe-flow interactions), determine the exchange of heat, momentum, and tracers between the lower atmosphere and upper ocean. Climate models do not represent either of these highly variable interactions. We use a novel, high-resolution, discrete element modeling framework to examine ice-ocean boundary layer (IOBL) turbulence within a domain approximately the size of a climate model grid. We show floe-scale effects could cause a marked increase in the production of fine-scale three-dimensional turbulence in the IOBL relative to continuum model approaches, and provide a method of representing that turbulence using bulk parameters related to the spatial variance of the ice and ocean: the floe size distribution and the ocean kinetic energy spectrum.

Plain Language Summary Sea ice is a complex broken mosaic of individual pieces, called floes. These floes control how heat and momentum move between the atmosphere and ocean. But these floes interact with each other as well as with the upper ocean and lower atmosphere, and this means that these exchanges can be complexly related to both types of processes: floe-floe and floe-flow. Using experiments that explicitly evolve sea ice floes interacting with each other and the upper ocean, we develop a formulation for how momentum is transferred between the ice and ocean as a function of simple parameters of the ice-ocean system that may be available to climate models.

1. Introduction

A key component of Earth's climate system, sea ice is a primary mediator of exchange across the atmosphere-ocean boundary in polar regions. Ongoing Arctic sea ice loss (e.g., Meier & Stroeve, 2022, and others) and changes in Antarctic sea ice (e.g., Eyras et al., 2021; Purich & Doddridge, 2023) therefore will lead to changes in air-sea coupling. The shift to a more seasonal Arctic sea ice regime and relative expansion of marginal ice zones (MIZs; Strong & Rigor, 2013; Rolph et al., 2020) may lead to increased ocean mixing (Rainville et al., 2011) due to the declining role of ice internal stress, which disrupts wind-momentum transfer (e.g., Brenner et al., 2021, 2023; Martin et al., 2014). That shift might modify Ekman pumping, ocean overturning, and freshwater storage in the Arctic Ocean (Wang et al., 2019; Wu et al., 2021). It also would alter sub-ice-surface oceanic eddy fields (Armitage et al., 2020) and mixed layer depths, which are regulated in part by frictional effects in the ice-ocean boundary layer (Cassianides et al., 2023; Gupta et al., 2020; Manucharyan & Thompson, 2022; Meneghello et al., 2020; Ou & Gordon, 1986).

Sea ice is a composite of pieces, called floes, that vary in size over scales from meters to tens of kilometers across (e.g., Horvat et al., 2019; Stern et al., 2018). Yet when considering air-sea coupling at climate model scales, the role of sea ice variability is typically collapsed to a single metric: the sea ice concentration (SIC), c . In models, the net ocean/atmosphere surface fluxes in a model grid cell are typically calculated through “flux-averaging” (e.g., Claussen, 1990). For some field, χ (e.g., heat, momentum), the net surface flux, F_χ is:

$$(F_\chi)_{\text{net}} = c(F_\chi)_{\text{io/ia}} + (1 - c)(F_\chi)_{\text{ao}}, \quad (1)$$

© 2023 The Authors.

This is an open access article under the terms of the [Creative Commons Attribution-NonCommercial License](https://creativecommons.org/licenses/by-nc/4.0/), which permits use, distribution and reproduction in any medium, provided the original work is properly cited and is not used for commercial purposes.

the ice concentration-weighted sum of the atmosphere-ocean (subscript *ao*) and ice-ocean/ice-atmosphere fluxes (subscript *io/ia*). However, when the floes are resolved, the concentration fields and concentration-weighted fluxes are a suitable measure only of the averaged conditions, not the pointwise conditions which vary intermittently due to the presence or absence of a floe.

It is well-known that a variety of exchange processes are heavily affected by floe-scale variability. *Floe-floe* interactions determine the evolution of sea ice through granular rheological laws for ice internal stresses within the MIZ (Feltham, 2008; Herman, 2013a; Shen et al., 1987), which remain an active area of research (e.g., Herman, 2022; Rynders et al., 2022) that is not implemented in current-generation climate models. Coupled interactions between floes and the ocean and atmosphere (*floe-flow* interactions) impact both atmospheric boundary layer and ice-ocean boundary layer (IOBL) processes (e.g., Gupta & Thompson, 2022; Horvat et al., 2016; Wenta & Herman, 2018, 2019). Additionally, ice-ocean and ice-atmosphere drag is highly dependent on sea ice geometry, but existing approaches for bulk formulations of air-sea momentum exchange (Lüpkes et al., 2012; Tsamados et al., 2014) fail to account for a variable distribution of floe sizes (Bateson, 2021; Brenner et al., 2021).

In this work, we explore the dual roles of floe-floe and floe-flow dynamics on ice-ocean exchange in the MIZ using a novel discrete element model of sea ice floe dynamics (Rabatel, 2015; Rabatel et al., 2015), forced by variable ocean currents that are derived from simulations of an ice edge with only air-sea heat fluxes and brine rejection, not wind stresses (Lo Piccolo, 2021; Lo Piccolo et al., 2023).

2. Background and Methods

2.1. Parameterization of Ice-Ocean Turbulent Exchange

Bulk drag laws parameterize local turbulent ocean-ice stress, τ_{oi} , in terms of differences between sea ice velocity \mathbf{u}_i and near-surface ocean velocity \mathbf{u}_o , via the ice-ocean relative velocity, $\mathbf{u}_{rel} = \mathbf{u}_o - \mathbf{u}_i$:

$$\tau_{oi} = \rho_o C_{io}(\mathbf{u}_{rel}) \|\mathbf{u}_{rel}\|, \quad (2)$$

where ρ_o is the ocean density and C_{io} is a turbulent transfer coefficient appropriate for the choice of ‘near-surface’ depth (McPhee, 1980).

Boundary stresses transfer energy from the relatively larger-scale ocean currents (including e.g., mesoscale/submesoscale eddies) to fine scale three-dimensional turbulence through shear production of turbulent kinetic energy (TKE):

$$\mathcal{P} = \tau \cdot \frac{\partial \mathbf{u}}{\partial z}, \quad (3)$$

where τ and \mathbf{u} are the vertically varying stress and velocity in the ocean (z is the vertical coordinate). Locally, \mathcal{P} is approximately balanced by small-scale viscous dissipation, ε (i.e., $\mathcal{P} \sim \varepsilon$), so boundary friction is a pathway to energy dissipation. Thus, friction damps variability in the ocean current field (e.g., Morison et al., 1985; Pinkel, 2005; Shrestha & Manucharyan, 2021; Manucharyan & Thompson, 2022; Brenner et al., 2023, and others).

Ocean-ice stress is transferred across a shallow ‘‘inner’’ boundary layer (with depth of a few meters; Shaw et al., 2008; Cole et al., 2017), often characterized as having a ‘‘law-of-the-wall’’-like structure (e.g., MCPhee, 2008; Shaw et al., 2008). Following the law-of-the-wall assumption (which gives that the stress within the layer is constant), the vertical integral of \mathcal{P} over this IOBL yields a total frictional production of TKE in terms bulk parameters (equivalent to the dissipation formula in Kohout et al., 2011; Herman et al., 2019):

$$S \equiv \int \mathcal{P} dz \sim \tau_{oi} \cdot \mathbf{u}_{rel} = \rho_o C_{io} \|\mathbf{u}_{rel}\|^3. \quad (4)$$

This formulation is consistent with observations of integrated turbulent dissipation within the marginal ice zone (Smith & Thomson, 2019).

Representation of sea ice as solid-body floes—as opposed to traditional continuum models (e.g., Golden et al., 2020)—introduces constraints on the ice velocity field, leading to production/dissipation of TKE that is

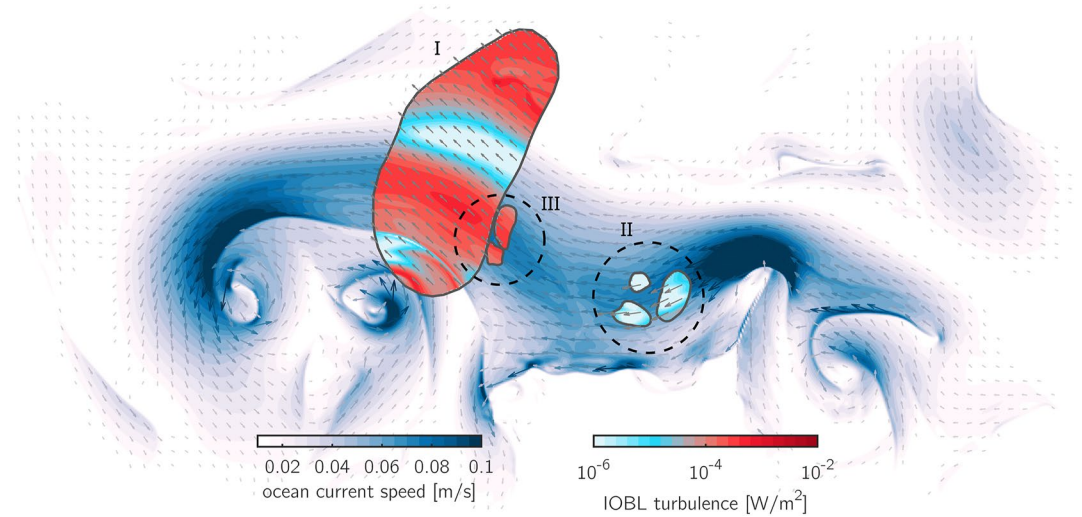


Figure 1. A schematic showing how scale mismatches between ocean flow (blue colormap and background vectors) and ice velocity (vector arrows over ice floes) contribute to IOBL shear production, S (cyan/red colormap).

highly dependent on the relative spatial scales of ice floes to ocean flow. Large floes compared to the scale of ocean variability generate more turbulence than small floes (cf., floes I and II in Figure 1) due to ice-ocean velocity mismatches over the size of the floe. Furthermore, collisions can limit correlated ice-ocean motion (floes III in Figure 1). In the work to follow, we will focus on understanding and parameterizing S .

2.2. Sea Ice Discrete Element Model

We use a discrete element model known as “FloeDyn,” which describes the dynamics of assemblies of individual sea ice floes (Rabatel, 2015; Rabatel et al., 2015). The floes act as rigid bodies that move in response to atmospheric or oceanic forcing and due to floe collisions. In between collisions, the translational and angular velocities, U_i and ω_i , respectively, for each ice floe are given by:

$$M \frac{dU_i}{dt} = M\mathcal{F} + \int_A (\tau_{ai} + \tau_{oi}) dA, \quad (5a)$$

$$I \frac{d\omega_i}{dt} = \int_A (\mathbf{x} - \mathbf{x}_c) \times (\tau_{ai} + \tau_{oi}) dA, \quad (5b)$$

where M is the mass of the floe, τ_{ai} and τ_{oi} are, respectively, the atmosphere-ice and ocean-ice stresses (in our simulations there are no wind stresses, so $\tau_{ai} = 0$), \mathcal{F} represents other external body forces, I is the moment of inertia, and \mathbf{x} is the horizontal position vector with \mathbf{x}_c the position of the floe centroid. While Rabatel et al. (2015) only include the body force, \mathcal{F} , associated with the Coriolis effect ($\mathcal{F}_c = -f\hat{k} \times U_i$, for \hat{k} the vertical unit normal vector and f the Coriolis parameter, $f = 1.4 \times 10^{-4} \text{ s}^{-1}$), we implemented an additional gravitational body force due to the mean sea surface tilt over a floe ($\mathcal{F}_g = \frac{1}{A} \int_A f\hat{k} \times \mathbf{u}_o dA$) and the total body force applied in Equation 5a is the combination of these two ($\mathcal{F} = \mathcal{F}_c + \mathcal{F}_g$).

Ice interactions are resolved separately from Equation 5. The model approximates inelastic collisions between floes as occurring over an infinitesimally small time, during which the momentum of each floe changes as $MU_i(t^+) = MU_i(t^-) + \sum \mathcal{I}$ (the times before and after collision $t^+ - t^- \rightarrow 0$). The set of impulses, \mathcal{I} , due to all contacts between any set of floes are modeled as a linear complimentary problem using Coulomb's law (see Rabatel et al., 2015, for further details).

Because floes move with the area-integrated stress, the leading-order steady-state solution to Equation 5a (found using a linear drag law, as in Leppäranta et al., 2012) gives the floe translation velocity as matching the mean ocean velocity under it: $U_i \sim \langle \mathbf{u}_o \rangle$ (where $\langle \cdot \rangle$ denotes the areal mean over a floe). Similarly, the angular velocity of a floe in steady-state matches the ocean vorticity field: $\omega_i \sim \frac{1}{2} \langle \zeta_o \rangle$ (where the factor of 1/2 arises due to the

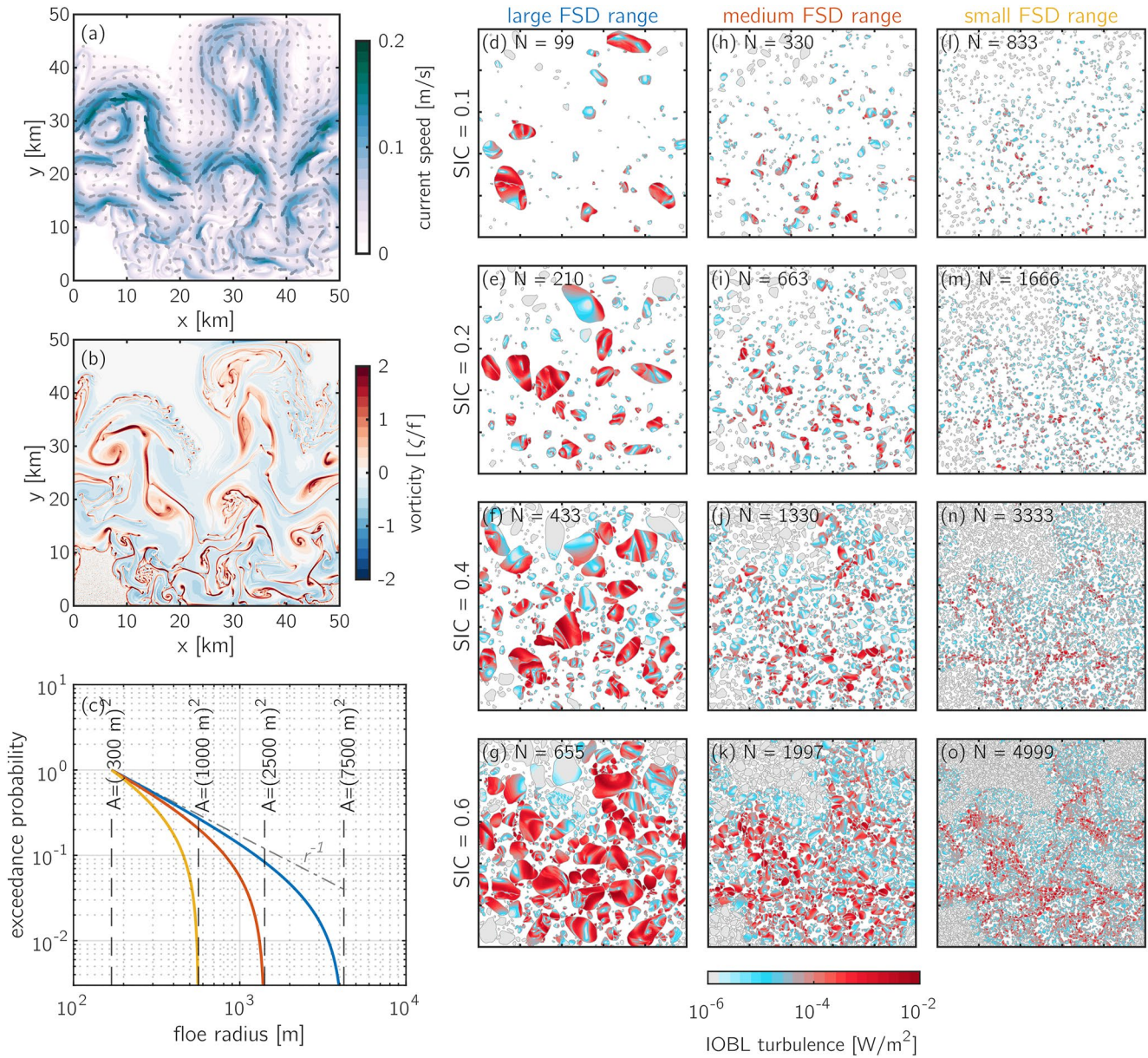


Figure 2. Snapshots of the ocean surface current velocity field (a) and associated vorticity (b) used to force the sea ice model. (c) Complementary cumulative distributions of number of floe sizes for the three different FSD cases tested. (d–o) Snapshots of sea ice floe configurations for the different FSD cases (columns) for example, SICs (rows) and associated fields of IOBL turbulence, S . Labels on each of the panels show the number of ice floes, N , for a given simulation.

relationship between angular velocity and vorticity), a fact that has been exploited in remote-sensing reconstructions of upper-ocean vorticity (Lopez-Acosta et al., 2019; Manucharyan et al., 2022).

2.3. Model Configuration and Experiments

We run a series of one-way forced FloeDyn experiments using ocean near-surface currents (specified at 1.25 m depth) provided by a separate ocean simulation. This ocean simulation (from Lo Piccolo, 2021; Lo Piccolo et al., 2023) uses the Massachusetts Institute of Technology general circulation model (MITgcm; Marshall et al., 1997) to investigate submesoscale energy transfers at a sea ice edge. It considers an ocean domain half-covered by sea ice and forced by a cold atmosphere, leading to rapid refreezing and brine rejection in the ice-free part of the domain. The resulting spatial gradient in buoyancy flux leads to an active eddy field (Figures 2a and 2b) as available potential energy (APE) is converted to eddy kinetic energy (EKE). We forced

FloeDyn with currents from a 5-day subset at the end of the ocean simulation (days 25–30) when eddies have saturated the domain, but include no thermodynamic effects or feedbacks to the ocean model.

Each FloeDyn simulation has the ocean surface randomly populated by sea ice floes of varying sizes and shapes. Here, floe size refers to the effective floe radius, r , defined in terms of floe surface area, A , as: $r = \sqrt{A/\pi}$. Floe sizes were selected following truncated power-law FSDs (e.g., Stern et al., 2018) with number density $N(r) = Cr^{-\alpha}$ in the interval $r \in [r_{\min}, r_{\max}]$, where $N(r)dr$ describes the number of floes per unit area with size between r and $r + dr$, and constant C chosen such that $\int_{r_{\min}}^{r_{\max}} (\pi r^2) N(r) dr = c$ (the SIC). For truncated distributions, the complementary cumulative distribution function is concave-down (Stern et al., 2018). We performed simulations over a range of SICs for three different FSDs. Each FSD had the same power-law exponent, $\alpha = 2$, and same minimum floe size, with varying maximum floe sizes (Figure 2c), defining “large”, “medium,” and “small” FSD cases. Floe shapes were selected from a library of shapes extracted from sea ice imagery (Rabatel et al., 2015), which include non-convex outlines. Mean caliper diameters ranged from $\sim 2r$ to $\sim 2.3r$. These shapes were discretized using an internal triangular mesh with equal-sized mesh elements. For each FSD, we tested fractional SICs in 0.1 increments from 0.1 to 0.8 (large FSD), 0.7 (medium), and 0.6 (small). The maximum SIC we examine is smaller for smaller FSD due to geometrical and numerical constraints. All floes were taken as having the same constant thickness of 1 m and ice-ocean drag coefficient $C_{io} = 5 \times 10^{-3}$. Other model parameters (e.g., the coefficient of restitution) were left at the default values used by Rabatel et al. (2015).

Ocean surface currents were supplied to FloeDyn within a $50 \text{ km} \times 50 \text{ km}$ periodic domain at a 50 m horizontal grid resolution and 4 hr temporal resolution. Currents were linearly interpolated (in space and time) to the locations of internal mesh points making up each sea ice floe at each calculation timestep. FloeDyn uses an adaptive timestepping mechanism to avoid floe interpenetration so calculation timesteps varied throughout each simulation, but a default timestep of 30 s is used in the absence of collisions. Model snapshot output is at each 1 hr, and sub-sampled to match the 4 hr ocean forcing. The first 8 hr of each simulation were discarded as a spin-up time as floes started from rest (similar to Manucharyan et al., 2022). Floe translational and rotational velocity outputs (\mathbf{U}_i and ω_i) and binary masks of the floe positions were then used to reconstruct the full ice velocity field on the input forcing grid at each timestep and an estimate of IOBL-integrated TKE production, S , was calculated following Equation 4. The process results in some discretization errors for the smallest ice floes, but we find this does not materially affect the results we present below.

2.4. Velocity Decomposition

To analyze aggregate results and understand grid-scale IOBL TKE production, we perform a floe-by-floe Reynolds-type decomposition of the ice-ocean relative velocity. Over each sea ice floe, ice and ocean velocity fields are separated into means and perturbations: $\mathbf{u} = \langle \mathbf{u} \rangle + \mathbf{u}'$. The spatially-varying ice velocity field, $\mathbf{u}_i(\mathbf{x})$, is a combination of the translational and angular motions of the floe: $\langle \mathbf{u}_i \rangle = \mathbf{U}_i$, and $\mathbf{u}'_i = \omega_i \hat{k} \times (\mathbf{x} - \mathbf{x}_c)$. The ice-ocean relative velocity for each floe can be written as:

$$\begin{aligned} \mathbf{u}_{rel} &= [\langle \mathbf{u}_o \rangle - \langle \mathbf{u}_i \rangle] + \mathbf{u}'_o - \mathbf{u}'_i \\ &= \boldsymbol{\delta}_{oi} + \mathbf{u}'_o - \mathbf{u}'_i, \end{aligned} \quad (6)$$

where $\boldsymbol{\delta}_{oi} \equiv [\langle \mathbf{u}_o \rangle - \mathbf{U}_i]$, the floe-mean ice-ocean velocity difference. Since we expect $\mathbf{U}_i \sim \langle \mathbf{u}_o \rangle$ for non-interacting floes (Section 2.2), the term $\boldsymbol{\delta}_{oi}$ primarily reflects translational velocity differences arising from floe-floe interactions. Those interactions can also impact floe rotation—the effects of which would be embedded in \mathbf{u}'_i .

When computing the local turbulence production, we note that Equation 4 depends on the relative velocity *magnitude*. Taking the floe-average of the inner product of Equation 6 with itself, we find:

$$\begin{aligned} \mathbf{u}'_i \ll (\boldsymbol{\delta}_{oi} + \mathbf{u}'_o) \\ \langle \|\mathbf{u}_{rel}\|^2 \rangle \sim \langle \|\boldsymbol{\delta}_{oi} + \mathbf{u}'_o\|^2 \rangle, \end{aligned} \quad (7a)$$

and

$$\begin{aligned} \langle \boldsymbol{\delta}_{oi} \cdot \mathbf{u}'_o \rangle \sim 0 \\ \langle \|\mathbf{u}_{rel}\|^2 \rangle \sim \langle \|\boldsymbol{\delta}_{oi}\|^2 \rangle + \langle \|\mathbf{u}'_o\|^2 \rangle, \end{aligned} \quad (7b)$$

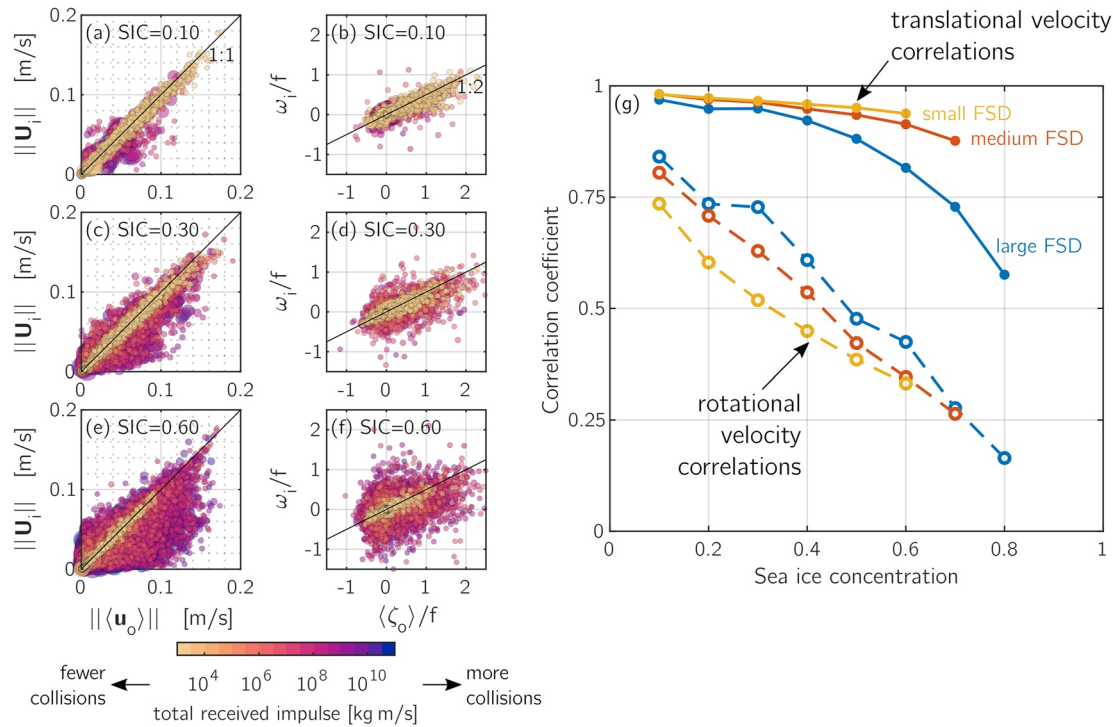


Figure 3. (a) Scatter plots comparing sea ice translational velocity (y-axis) to floe-averaged ocean velocity (x-axis) for a low SIC simulation with the large FSD. (b) Same, for rotational velocities. (c,d; e,f) Same as (a,b) but for 30% SIC or 60% SIC. Colors are cumulative received impulse, a measure of total collisional momentum imparted to each floe. (g) Floe ensemble-average correlation of (solid) translational motions and (dashed) rotational motions as a function of SIC and FSD.

where we have neglected the (small, see below) rotational term, and assumed that δ_{oi} and \mathbf{u}'_o are uncorrelated. Thus Equation 7 partitions the average relative velocity magnitude into separate contributions from *floe-floe interactions* and *floe-flow interactions*. As shown in Equation 4, the relative velocity magnitude is the key agent for production of IOBL turbulence. Section 3.3 will introduce scaling to relate $\langle \|\mathbf{u}_{rel}\|^2 \rangle$ to $\langle \|\mathbf{u}_{rel}\|^3 \rangle$ (the quantity of interest for Equation 4).

3. Results

3.1. Coupling Between Ice Floe Velocities and Ocean Currents

The leading order solutions of Equation 5 suggest that non-interacting floes move with the floe-mean ocean current field: $\mathbf{U}_i \sim \langle \mathbf{u}_o \rangle$ and $\omega_i \sim \frac{1}{2} \langle \zeta_o \rangle$ (Section 2.2). In low SIC simulations, floe velocities generally matched these solutions (Figures 3a and 3b). Deviations from the expected leading-order solutions were primarily observed for floes impacted by collisions (using cumulative impulse magnitude received by a floe as a measure of the intensity of collisions, with redder colors indicating more intense collisions).

As SIC increases, an increase in collisions causes greater decoupling between sea ice and ocean velocities (Figures 3c–3f). Yet at all SICs, a subset of floes have ice velocities highly correlated with floe-averaged ocean velocities (tan-colored points concentrated on the 1:1 or 1:2 lines in Figures 3a–3f).

Correlation coefficients between ice and ocean velocities provide bulk measures of ice-ocean dynamic coupling. For translational velocities, the correlations between $\langle \mathbf{u}_o \rangle$ and \mathbf{U}_i over all floes in each simulation (solid lines in Figure 3g) are taken as the magnitude of the complex correlation (Kundu, 1976). At low SICs, $\langle \mathbf{u}_o \rangle$ and \mathbf{U}_i are highly correlated for all FSDs (e.g., correlation coefficients of ~ 0.98 for SIC = 0.1). As SIC increases, the correlations diverge for the different FSD cases, with a greater decline for the large FSD range compared to the small and medium cases. Correlations for rotational motion ($\langle \zeta_o \rangle$, ω_i ; dashed lines) are lower than for translational motions, even at low SIC, and degrade more rapidly with increasing SIC. These simulations highlight meaningful sea ice dynamic interaction forces for SIC below 0.80 that are highly dependent on both SIC and the FSD.

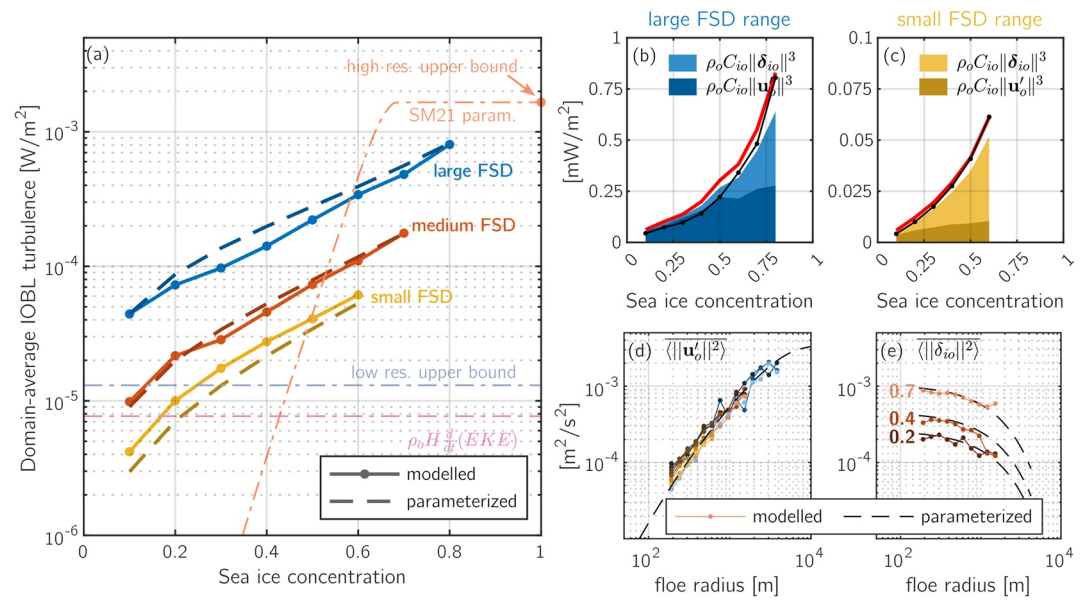


Figure 4. (a) Domain-averaged turbulent production, \tilde{S} , for the different FSD ranges (as labeled); solid lines represent model values and dashed lines represent parameterized values. Additional dashed-dot lines relate to contextual values discussed in the text. (b,c) Stacked-area plots showing the relative contributions of ocean dynamics and ice dynamics to \tilde{S} for the large/small FSD cases, with black curves showing the total from panel a, and red curves showing \tilde{S} calculated using $S = \rho_o C_{io} \|\delta_{io} + \mathbf{u}'_o\|^3$. (d,e) Bin-averaged and parameterized values of (d) the floe-size-dependent ocean variance (points colored by FSD range as in panel a, and shaded from dark to light for different SIC cases), and (e) examples from the medium FSD case of the floe-size and SIC dependent $\langle \|\delta_{oi}\|^2 \rangle$ (fractional SICs labeled).

3.2. IOBL Turbulence

IOBL TKE production, S , varies across the simulations. The domain-averaged TKE production \tilde{S} (where $\tilde{\cdot}$ denotes a domain-mean) exponentially increases with SIC for all three FSDs (Figure 4a, solid lines), but has considerably different magnitudes for each. The large FSD case has an order-of-magnitude higher \tilde{S} than the small FSD case. Within each simulation, there is also variability in the TKE production field (Figures 2d–2o). For low SIC simulations (Figures 2d, 2h, and 2l), there is a clear difference in TKE production across floe sizes: S is significantly enhanced for larger floes. As SIC increases, there is an increase in the turbulence associated with smaller floes so that there is no longer a clear division of S by floe size (Figures 2g, 2k, and 2o). High turbulence production in the small FSD case is largely confined to zones of oceanic convergence (Figure 2o), which in turn is a characteristic of the submesoscale flow (D’Asaro et al., 2018). As seen in Figures 2d–2o, the scale-dependence of S emerges from the statistical mean over many floes—the TKE production over any individual floe is heavily influenced by its location relative to the energetic ocean currents.

We examine the dual contributions of ocean variability and floe collisions to \tilde{S} by calculating turbulent production using, respectively, $\rho_o C_{io} \|\mathbf{u}'_o\|^3$ and $\rho_o C_{io} \|\delta_{io}\|^3$ in place of Equation 4 (Figures 4b and 4c). For low SIC, ice dynamics had a minimal impact on the IOBL turbulence for all FSDs, consistent with the low occurrence of collisions (Section 3.1, Figures 3a and 3b). In these low SIC ranges, \tilde{S} primarily results from ocean dynamics contributions. As those contributions depend strongly on the floe scale relative to eddy scale (Figure 1), the separation of \tilde{S} for different FSD cases in Figure 4a can be attributed almost entirely to \mathbf{u}'_o . Increasing SIC is accompanied by an exponential increase in the turbulence associated with ice dynamics for all FSDs, while ocean dynamics effects only scale linearly with SIC. We note that $\rho_o C_{io} \|\delta_{io}\|^3 + \rho_o C_{io} \|\mathbf{u}'_o\|^3 \neq \rho_o C_{io} \|\delta_{io} + \mathbf{u}'_o\|^3$ (the latter shown as red lines).

The relatively small residual between the combined contributions, calculated from $\rho_o C_{io} \|\delta_{io} + \mathbf{u}'_o\|^3$ (red lines), and the total (black lines) confirms that the rotation term in Equation 6 is of secondary importance, as assumed in Equation 7.

3.3. A Framework for Parameterizing IOBL Turbulence Production

A scaling framework for the total IOBL TKE production follows from Equation 4 with the decomposition in Equation 7. Together, we use them to give an expression for the average TKE production for each floe (indexed by n). Then floe-average and domain total S (respectively $\langle S \rangle_n$, and S_{total}) are:

$$\langle S \rangle_n \sim \rho_o C_{io} \left[\langle \|\mathbf{u}'_o\|^2 \rangle_n + \langle \|\delta_{io}\|^2 \rangle_n \right]^{3/2}, \quad (8a)$$

$$S_{\text{total}} \equiv \sum_n (A_n \langle S \rangle_n), \quad (8b)$$

where $A_n = \pi r_n^2$ is the area of floe n . In Equation 8a we make the scaling approximation $\langle \|\mathbf{u}_{rel}\|^3 \rangle \sim \langle \|\mathbf{u}_{rel}\|^2 \rangle^{3/2}$. For the present simulations, this approximation underestimates $\langle \|\mathbf{u}_{rel}\|^3 \rangle$ by an average of $\sim 3\%$ – 10% . Defining $\overline{\langle \rangle}$ as an ensemble average over many floes of the same size, we rewrite Equations 8a and 8b as:

$$\overline{\langle S \rangle}(r) \sim \gamma \rho_o C_{io} \left[\overline{\langle \|\mathbf{u}'_o\|^2 \rangle} + \overline{\langle \|\delta_{io}\|^2 \rangle} \right]^{3/2}. \quad (9a)$$

$$S_{\text{total}} \equiv \mathcal{A} \int_0^\infty \pi r^2 N(r) \overline{\langle S \rangle}(r) dr, \quad (9b)$$

where \mathcal{A} is the domain area and γ is a correction factor, to account for the differences between $\overline{\langle \|\mathbf{u}_{rel}\|^2 \rangle^{3/2}}$ and $\overline{\langle \|\mathbf{u}_{rel}\|^2 \rangle}^{3/2}$. The correction factor depends on the statistical properties of $\langle \|\mathbf{u}_{rel}\|^2 \rangle$. Here, on the basis that $\langle \|\mathbf{u}_{rel}\|^2 \rangle$ approximately fits an exponential distribution, it is $\gamma = 3\sqrt{\pi}/4$. Because Equation 9a constructed S as an ensemble value over all floes of the same size, we were able to recast Equation 8b in terms of the FSD, $N(r)$, in Equation 9b.

3.3.1. Scaling Ocean Variability

From the relative velocity decomposition (Equation 7b), we see that $\langle \|\mathbf{u}'_o\|^2 \rangle$, is the variance of the ocean current field over an individual sea ice floe. Again taking the ensemble average of all floes of size r , we may relate this floe-scale variance to the ocean kinetic energy spectral density. The one-dimensional spectrum, $E(k)$ describes the variance in ocean currents for each wavenumber, k . Thus, a parameterization for $\overline{\langle \|\mathbf{u}'_o\|^2 \rangle}$ for a given floe size, r , is based on an appropriate high-pass-filtered spectrum:

$$\mathbb{P}_o(r) \equiv \overline{\langle \|\mathbf{u}'_o\|^2 \rangle} = \int_0^\infty [1 - \text{sinc}^2(rk)] E(k) dk, \quad (10)$$

where the shape of the high-pass filter reflects that floes are spatial “boxcar” filters of the ocean velocity variance.

Over the full range of simulations, we show in Figure 4d that $\overline{\langle \|\mathbf{u}'_o\|^2 \rangle}$ is well predicted by the parameterization $\mathbb{P}_o(r)$ when using the calculated ocean current spectrum. Due to convergence in the ocean currents, floes are not evenly distributed in space, and instead preferentially sample more energetic regions; however, this effect is negligibly small but depends on the Rossby number of the flow (D’Asaro et al., 2018).

We note that the separation of inertial ranges in $E(k)$ that can occur below and above the ocean deformation radius (as in 2D quasigeostrophic turbulence) would imprint on $\mathbb{P}_o(r)$, and thus lead to a potential regime shift in variability across floe sizes (e.g., as seen in Gupta & Thompson, 2022).

3.3.2. Scaling Ice Interactions

The remaining part of S is δ_{oi} . This relates to the internal stress dynamics of the sea ice pack, and the correlation of local floe motions with the ocean flow. Within the SIC ranges considered here (≤ 0.8), ice is often considered to be in “free drift,” and internal stress dynamics are thought to be negligible. However, as seen in Section 3.1, δ_{oi} is non-zero across the simulations, highlighting that mechanical aspects of sea ice can be important even below SIC ~ 0.8 . The theory of how to relate floe-scale mean velocities and ocean velocities is a subject of active research into sea ice granular rheology (e.g., Herman, 2022) and beyond the scope of the present study.

Still, as shown in Figure 3g, decoupling of the floe-mean ice-ocean velocities due to ice interaction forces varies with both SIC and FSD—and across simulations we obtain empirical fits to $\overline{\langle \|\delta_{io}\|^2 \rangle}$ of the form:

$$\mathbb{D}(r) \equiv \overline{\langle \|\delta_{io}\|^2 \rangle} \propto \exp(a_1 c + a_2 r), \quad (11)$$

(Figure 4e), for constants a_1 and a_2 that vary as a function of FSD.

The “representative floe size,” defined as

$$R \equiv \frac{\int r^3 N(r) dr}{\int r^2 N(r) dr}, \quad (12)$$

was identified as a useful metric of the size distribution of ice floes (Horvat & Tziperman, 2017; Horvat et al., 2019; Roach et al., 2018), and has been used in proposed rheological laws for polydisperse granular media (Herman, 2022). Based on this concept, we employ R to fit the parameters: $a_1 = 0.73R^{0.2}$ and $a_2 = -0.42R^{-1}$ in Equation 11. This method is applicable to the “narrow” power-law-type FSDs examined in this study, but future work will be necessary to gauge the general applicability of this fit to, for example, FSDs spanning a wider floe size range, or other FSD shapes (e.g., log-normal type distributions; Mokus & Montiel, 2022).

Above some SIC threshold ($\gtrsim 0.8-0.9$), we expect a critical transition in ice interaction dynamics (i.e., a “jamming transition”; Herman, 2013b). Beyond this threshold, it is unlikely that the scaling in Equation 11 would apply.

3.3.3. Putting It All Together

Combining Equations 9a and 9b with Equations 10 and 11, we now can estimate \tilde{S} using bulk, integrated quantities of the sea ice floe field and the ocean flow field. We write:

$$\frac{S_{\text{total}}}{\mathcal{A}} = \gamma \rho_o C_{io} \int \pi r^2 N(r) [\mathbb{P}_o(r) + \mathbb{D}(r)]^{3/2} dr \quad (13)$$

which, for functional forms of \mathbb{P}_o and \mathbb{D} , could be evaluated as an expression of bulk FSD descriptors (r_{\min} , r_{\max} and α). These estimates approximate the scaling and magnitude of the overall model results (dashed lines in Figure 4a), despite a number of simplifying assumptions.

4. Discussion

Here we have provided a framework for a simple parameterization of the magnitude and scaling of IOBL turbulence due to ice-ocean interactions across a range of floe sizes and within sea ice concentration ranges traditionally associated with “free-drift” conditions. The parameterization (Equation 13) is applicable to a region comparable to a GCM grid cell, and represents the *floe-floe* and *floe-flow* interactions that give rise to ocean drag and turbulence. The IOBL turbulence is a scale-dependent sink of larger-scale kinetic energy (e.g., from mesoscale/submesoscale currents), and would be unresolved in low resolution continuum models.

The importance of understanding this scale-dependence can be illustrated by comparing \tilde{S} to estimates that could be calculated at the GCM grid scale by traditional models. For example, an upper bound can be found by assuming fixed sea ice ($\mathbf{u}_i = 0$) at 100% SIC, and using the domain-mean ocean velocity, so $\mathbf{u}_{rel} = \tilde{\mathbf{u}}_o$ in Equation 4. This upper limit (Figure 4a, purple line) is nearly two orders-of-magnitude lower than the maximum \tilde{S} in our simulations, and significantly less than \tilde{S} across the majority of the simulations (except for low SICs with the small FSD case). Thus, floe-scale effects on surface flux can lead to significantly enhanced sub-grid-scale IOBL turbulence that needs to be parameterized to be able to include it in GCMs. This IOBL turbulence is involved in ice-ocean heat flux, mixing of the upper oceans, deepening of the oceanic boundary layers, entrainment of deeper waters (conceivably including subsurface thermal maxima, e.g., Pham et al., 2023), and the shear within the upper ocean.

Using a high-resolution continuum sea ice-ocean coupled model, Shrestha and Manucharyan (2021) showed that the classic Fox-Kemper et al. (2008) parameterization for mixed-layer eddies (MLEs) was suppressed for high sea ice concentrations. They suggest a modification of the MLE scheme based on IOBL turbulent dissipation, ε , parameterized as a function of SIC. As the scaling in Shrestha and Manucharyan (2021) assumes $\mathbf{u}_i = 0$ as $\text{SIC} \rightarrow 1$, we employ that assumption in re-dimensionalizing their parameterization (peach-colored SM21 line in Figure 4a) by setting $[\int \varepsilon dz]_{c=1} = \tilde{\varepsilon}$ as calculated using $\mathbf{u}_{rel} = \mathbf{u}_o$ (the full, high-resolution ocean current field) in Equation 4. Thus, the value at $\text{SIC} = 1$ represents a high-resolution upper bound on the $\tilde{\varepsilon}$. The TKE production \tilde{S} in most of our simulations exceeds the kinetic energy flux into MLEs ($\rho_o H \frac{d}{dt} EKE$ where H is the mixed layer depth) in the ocean model from which the forcing was derived (Figure 4a, pink line) (Lo Piccolo et al., 2023),

suggesting that those eddies may be similarly suppressed if we were using a coupled model. However, floe-scale effects introduce a marked difference in the SIC dependence of TKE production in our model relative to the dissipation parameterization of Shrestha and Manucharyan (2021). In continuum ice models, ice strength (and associated interaction forces) is negligibly small below SIC ~ 0.8 ; however, explicit representation of sea ice floes here showed that ice dynamic interactions impact ice-ocean coupling even below this SIC cutoff in a way that depends on the FSD (Section 3.1).

Equation 13 uses two inputs to parameterize IOBL turbulence: the ocean kinetic energy spectrum, $E(k)$, and the FSD. Here, we directly resolve the ocean currents, and hence $E(k)$ in Equation 10; however, in a GCM, the sub-grid ocean energy spectrum is not evolved. Fox-Kemper and Menemenlis (2008) suggest methods to assess the total sub-grid variance using grid-scale resolved quantities. With these methods—together with existing understanding of sub-ice ocean variance spectrum (e.g., Timmermans et al., 2012; Timmermans & Marshall, 2020) or general ocean turbulence (e.g., Fox-Kemper et al., 2011)—it may be possible to estimate the sub-grid variance necessary for Equation 13. In contrast to $E(k)$, a prognostic FSD is now evolved in several operational-quality GCMs (e.g., Boutin et al., 2022; Roach et al., 2018, 2019), which could be used directly in Equations 11 and 13. For GCMs lacking this functionality, it may be possible to instead use simplified concentration-based estimate of the FSD (e.g., Perovich & Jones, 2014).

Generalization of the parameterization presented here will require some additional effort. The exponential increase in ice strength at high SIC ($\gtrsim 0.8$ – 0.9) suggested by continuum models (Hibler, 1979) implies a critical transition in ice interaction forces (e.g., Herman, 2013b). To extend our findings to higher SIC values, we need to expand Equation 11 accordingly. As SIC $\rightarrow 1$, $\tilde{\sigma}$ should converge to a limit independent of the FSD (the FSD is ill-defined for SIC = 1). However, extrapolation of the current Equation 13 fails to reproduce this behavior (Figure 4a). The present results are also limited by the use of one-way coupling between the ocean and the sea ice. Before implementation of the parameterization, work with future two-way ice-ocean coupled configurations is needed to investigate impacts on spectral shape due to both suppression of MLEs under sea ice (Manucharyan & Thompson, 2022; Shrestha & Manucharyan, 2021), and energization of MLEs due to buoyancy flux at floe edges (Gupta & Thompson, 2022; Horvat et al., 2016), and mixing and vertical momentum transport due to the IOBL turbulence driven by the effects studied here. These effects will impact the shape of the energy spectra, $E(k)$ used in Equation 10 in as-yet unknown ways that require consideration.

Despite these limitations, this study highlights the need to consider scale-dependent effects of sea ice floes on ice-ocean coupling and surface fluxes. We provide a launching point for parameterizing the associated IOBL fluxes of energy based on a floe-scale Reynolds decomposition that separates ice dynamic and ocean dynamic effects on relative velocity. We anticipate that this floe-scale averaging has promise for applicability in all mediated air-sea exchanges, which we propose to continue in future work.

Data Availability Statement

All data are available through the Brown Digital Repository (<https://repository.library.brown.edu/>). Data from the ocean simulation used to force FloeDyn are available in Lo Piccolo, Horvat, Christopher, & Fox-Kemper, Baylor (2023). Output data from the FloeDyn simulations are available in Brenner (2023).

References

- Armitage, T. W. K., Manucharyan, G. E., Petty, A. A., Kwok, R., & Thompson, A. F. (2020). Enhanced eddy activity in the Beaufort Gyre in response to sea ice loss. *Nature Communications*, 11(1), 761. <https://doi.org/10.1038/s41467-020-14449-z>
- Bateson, A. W. (2021). *Fragmentation and melting of the seasonal sea ice cover*. Doctoral dissertation, University of Reading. <https://doi.org/10.48683/1926.00098821>
- Boutin, G., Williams, T., Horvat, C., & Brodeau, L. (2022). Modelling the Arctic wave-affected marginal ice zone: A comparison with ICESat-2 observations. *Philosophical Transactions of the Royal Society A: Mathematical, Physical & Engineering Sciences*, 380(2235), 20210262. <https://doi.org/10.1098/rsta.2021.0262>
- Brenner, S. (2023). Data for Scale-dependent air-sea exchange in the polar oceans: Floe-floe and floe-flow coupling in the generation of ice-ocean boundary layer turbulence [Dataset]. Brown University. <https://doi.org/10.26300/R11S-ZG91>
- Brenner, S., Rainville, L., Thomson, J., Cole, S., & Lee, C. (2021). Comparing observations and parameterizations of ice-ocean drag through an annual cycle across the Beaufort Sea. *Journal of Geophysical Research: Oceans*, 126(4), e2020JC016977. <https://doi.org/10.1029/2020JC016977>
- Brenner, S., Thomson, J., Rainville, L., Crews, L., & Lee, C. (2023). Wind-driven motions of the ocean surface mixed layer in the Western Arctic. *Journal of Physical Oceanography*, 53(7), 1787–1804. <https://doi.org/10.1175/JPO-D-22-0112.1>
- Cassianides, A., Lique, C., Tréguier, A.-M., Meneghello, G., & De Marez, C. (2023). Observed spatio-temporal variability of the eddy-sea ice interactions in the Arctic Basin. *Journal of Geophysical Research: Oceans*, 128(6), e2022JC019469. <https://doi.org/10.1029/2022JC019469>

Acknowledgments

All authors on this project are supported through the Scale Aware Sea Ice Project (SASIP). SASIP is supported by Schmidt Futures, a philanthropic initiative that seeks to improve societal outcomes through the development of emerging science and technologies. ALP and BFK have partial support from NSF 2149041. Computing resources were provided by NSF 1655221.

- Claussen, M. (1990). Area-averaging of surface fluxes in a neutrally stratified, horizontally inhomogeneous atmospheric boundary layer. *Atmospheric Environment, Part A: General Topics*, 24(6), 1349–1360. [https://doi.org/10.1016/0960-1686\(90\)90041-K](https://doi.org/10.1016/0960-1686(90)90041-K)
- Cole, S. T., Toole, J. M., Lele, R., Timmermans, M.-L., Gallaher, S. G., Stanton, T. P., et al. (2017). Ice and ocean velocity in the Arctic marginal ice zone: Ice roughness and momentum transfer. *Elementa: Science of the Anthropocene*, 5, 55. <https://doi.org/10.1525/elementa.241>
- D'Asaro, E. A., Shcherbina, A. Y., Klymak, J. M., Molemaker, J., Novelli, G., Guigand, C. M., et al. (2018). Ocean convergence and the dispersion of flotsam. *Proceedings of the National Academy of Sciences*, 115(6), 1162–1167. <https://doi.org/10.1073/pnas.1718453115>
- Eayrs, C., Li, X., Raphael, M. N., & Holland, D. M. (2021). Rapid decline in Antarctic sea ice in recent years hints at future change. *Nature Geoscience*, 14(7), 460–464. <https://doi.org/10.1038/s41561-021-00768-3>
- Feltham, D. L. (2008). Sea ice rheology. *Annual Review of Fluid Mechanics*, 40(1), 91–112. <https://doi.org/10.1146/annurev.fluid.40.1.91>
- Fox-Kemper, B., Danabasoglu, G., Ferrari, R., Griffies, S. M., Hallberg, R. W., Holland, M. M., et al. (2011). Parameterization of mixed layer eddies. III: Implementation and impact in global ocean climate simulations. *Ocean Modelling*, 39(1), 61–78. <https://doi.org/10.1016/j.ocemod.2010.09.002>
- Fox-Kemper, B., Ferrari, R., & Hallberg, R. (2008). Parameterization of mixed layer eddies. Part I: Theory and diagnosis. *Journal of Physical Oceanography*, 38(6), 1145–1165. <https://doi.org/10.1175/2007JPO3792.1>
- Fox-Kemper, B., & Menemenlis, D. (2008). Can large eddy simulation techniques improve mesoscale-rich ocean models? In M. Hecht & H. Hasumi (Eds.), *Ocean modeling in an edying regime* (Vol. 177, pp. 319–338). AGU Geophysical Monograph Series.
- Golden, K. M., Bennets, L. G., Cherkaev, E., Eisenman, I., Feltham, D., Horvat, C., et al. (2020). Modeling sea ice. *Notices of the American Mathematical Society*, 67(10), 1. <https://doi.org/10.1090/noti2171>
- Gupta, M., Marshall, J., Song, H., Campin, J.-M., & Meneghello, G. (2020). Sea-ice melt driven by ice-ocean stresses on the mesoscale. *Journal of Geophysical Research: Oceans*, 125(11), e2020JC016404. <https://doi.org/10.1029/2020JC016404>
- Gupta, M., & Thompson, A. F. (2022). Regimes of sea-ice floe melt: Ice-ocean coupling at the submesoscales. *Journal of Geophysical Research: Oceans*, n/a(n/a), e2022JC018894. <https://doi.org/10.1029/2022JC018894>
- Herman, A. (2013a). Numerical modeling of force and contact networks in fragmented sea ice. *Annals of Glaciology*, 54(62), 114–120. <https://doi.org/10.3189/2013AoG62A055>
- Herman, A. (2013b). Shear-jamming in two-dimensional granular materials with power-law grain-size distribution. *Entropy*, 15(11), 4802–4821. <https://doi.org/10.3390/e15114802>
- Herman, A. (2022). *Granular effects in sea ice rheology in the marginal ice zone*. Phil Trans R Soc A(MIZ).
- Herman, A., Cheng, S., & Shen, H. H. (2019). Wave energy attenuation in fields of colliding ice floes – Part I: Discrete-element modelling of dissipation due to Ice–Water drag. *The Cryosphere*, 13(11), 2887–2900. <https://doi.org/10.5194/tc-13-2887-2019>
- Hibler, W. D. (1979). A dynamic thermodynamic sea ice model. *Journal of Physical Oceanography*, 9(4), 815–846. [https://doi.org/10.1175/1520-0485\(1979\)009<0815:ADTSIM>2.0.CO;2](https://doi.org/10.1175/1520-0485(1979)009<0815:ADTSIM>2.0.CO;2)
- Horvat, C., Roach, L. A., Tilling, R., Bitz, C. M., Fox-Kemper, B., Guider, C., et al. (2019). Estimating the sea ice floe size distribution using satellite altimetry: Theory, climatology, and model comparison. *The Cryosphere*, 13(11), 2869–2885. <https://doi.org/10.5194/tc-13-2869-2019>
- Horvat, C., & Tziperman, E. (2017). The evolution of scaling laws in the sea ice floe size distribution. *Journal of Geophysical Research: Oceans*, 122(9), 7630–7650. <https://doi.org/10.1002/2016JC012573>
- Horvat, C., Tziperman, E., & Campin, J.-M. (2016). Interaction of sea ice floe size, ocean eddies, and sea ice melting. *Geophysical Research Letters*, 43(15), 8083–8090. <https://doi.org/10.1002/2016GL069742>
- Kohout, A. L., Meylan, M. H., & Plew, D. R. (2011). Wave attenuation in a marginal ice zone due to the bottom roughness of ice floes. *Annals of Glaciology*, 52(57), 118–122. <https://doi.org/10.3189/172756411795931525>
- Kundu, P. K. (1976). Ekman veering observed near the ocean bottom. *Journal of Physical Oceanography*, 6(2), 238–242. [https://doi.org/10.1175/1520-0485\(1976\)006<0238:EVONTO>2.0.CO;2](https://doi.org/10.1175/1520-0485(1976)006<0238:EVONTO>2.0.CO;2)
- Leppäranta, M., Oikkonen, A., Shirasawa, K., & Fukamachi, Y. (2012). A treatise on frequency spectrum of drift ice velocity. *Cold Regions Science and Technology*, 76–77, 83–91. <https://doi.org/10.1016/j.coldregions.2011.12.005>
- Lopez-Acosta, R., Schodlok, M. P., & Wilhelmus, M. M. (2019). Ice Floe Tracker: An algorithm to automatically retrieve Lagrangian trajectories via feature matching from moderate-resolution visual imagery. *Remote Sensing of Environment*, 234(October), 111406. <https://doi.org/10.1016/j.rse.2019.111406>
- Lo Piccolo, A. (2021). *Arctic ocean submesoscale brine driven eddies: Modeling of a sea ice edge front (Tesi di laurea)*. University of Bologna.
- Lo Piccolo, A., Horvat, C., & Fox-Kemper, B. (2023). Energetics and transfer of submesoscale brine driven eddies at a sea ice edge. [Paper Submitted for Publication].
- Lo Piccolo, A., Horvat, C., Fox-Kemper, & Baylor (2023). Data for Energetics and transfer of submesoscale brine driven eddies at a sea ice edge [Dataset]. Brown University. <https://doi.org/10.26300/AK1P-2V10>
- Lüpkes, C., Gryanik, V. M., Hartmann, J., & Andreas, E. L. (2012). A parametrization, based on sea ice morphology, of the neutral atmospheric drag coefficients for weather prediction and climate models. *Journal of Geophysical Research*, 117(13), D13112. <https://doi.org/10.1029/2012JD017630>
- Manucharyan, G. E., Lopez-Acosta, R., & Wilhelmus, M. M. (2022). Spinning ice floes reveal intensification of mesoscale eddies in the western Arctic Ocean. *Scientific Reports*, 12(1), 7070. <https://doi.org/10.1038/s41598-022-10712-z>
- Manucharyan, G. E., & Thompson, A. F. (2022). Heavy footprints of upper-ocean eddies on weakened Arctic sea ice in marginal ice zones. *Nature Communications*, 13(1), 2147. <https://doi.org/10.1038/s41467-022-29663-0>
- Marshall, J., Adcroft, A., Hill, C., Perelman, L., & Heisey, C. (1997). Hydrostatic, quasi-hydrostatic and nonhydrostatic ocean modeling. *Journal of Geophysical Research*, 102(C3), 5733–5752. <https://doi.org/10.1029/96jc02776>
- Martin, T., Steele, M., & Zhang, J. (2014). Seasonality and long-term trend of Arctic Ocean surface stress in a model. *Journal of Geophysical Research: Oceans*, 119(3), 1723–1738. <https://doi.org/10.1002/2013JC009425>
- McPhee, M. G. (1980). An analysis of pack ice drift in summer. *Sea Ice Processes and Models*, 62–75.
- McPhee, M. G. (2008). *Air-ice-ocean interaction: Turbulent ocean boundary layer exchange processes*. Springer-Verlag. <https://doi.org/10.1007/978-0-387-78335-2>
- Meier, W., & Stroeve, J. (2022). An updated assessment of the changing Arctic Sea ice cover. *Oceanography*. <https://doi.org/10.5670/oceanog.2022.114>
- Meneghello, G., Doddridge, E., Marshall, J., Scott, J., & Campin, J.-M. (2020). Exploring the role of the “ice–ocean governor” and mesoscale eddies in the equilibration of the Beaufort gyre: Lessons from observations. *Journal of Physical Oceanography*, 50(1), 269–277. <https://doi.org/10.1175/JPO-D-18-0223.1>
- Mokus, N. G. A., & Montiel, F. (2022). Wave-triggered breakup in the marginal ice zone generates lognormal floe size distributions: A simulation study. *The Cryosphere*, 16(10), 4447–4472. <https://doi.org/10.5194/tc-16-4447-2022>

- Morison, J. H., Long, C. E., & Levine, M. D. (1985). Internal wave dissipation under sea ice. *Journal of Geophysical Research*, *90*(C6), 11959–11966. <https://doi.org/10.1029/JC090iC06p11959>
- Ou, H. W., & Gordon, A. L. (1986). Spin-down of baroclinic eddies under sea ice. *Journal of Geophysical Research*, *91*(C6), 7623–7630. <https://doi.org/10.1029/JC091iC06p07623>
- Perovich, D. K., & Jones, K. F. (2014). The seasonal evolution of sea ice floe size distribution. *Journal of Geophysical Research: Oceans*, *119*(12), 8767–8777. <https://doi.org/10.1002/2014JC010136>
- Pham, H. T., Sarkar, S., Johnson, L., Fox-Kemper, B., Sullivan, P. P., & Li, Q. (2023). Multi-scale temporal variability of turbulent mixing during a monsoon intra-seasonal oscillation in the Bay of Bengal: An LES study. *Journal of Geophysical Research: Oceans*, *128*(1), e2022JC018959. <https://doi.org/10.1029/2022JC018959>
- Pinkel, R. (2005). Near-inertial wave propagation in the western Arctic. *Journal of Physical Oceanography*, *35*(5), 645–665. <https://doi.org/10.1175/JPO2715.1>
- Purich, A., & Doddridge, E. W. (2023). Record low Antarctic sea ice coverage indicates a new sea ice state. *Communications Earth & Environment*, *4*(1), 1–9. <https://doi.org/10.1038/s43247-023-00961-9>
- Rabatel, M. (2015). *Modélisation dynamique d'un assemblage de floes rigides (Unpublished doctoral dissertation)*. Université Grenoble Alpes.
- Rabatel, M., Labbé, S., & Weiss, J. (2015). Dynamics of an assembly of rigid ice floes. *Journal of Geophysical Research: Oceans*, *120*(9), 5887–5909. <https://doi.org/10.1002/2015JC010909>
- Rainville, L., Lee, C., & Woodgate, R. A. (2011). Impact of wind-driven mixing in the Arctic Ocean. *Oceanography*, *24*(3), 136–145. <https://doi.org/10.5670/oceanog.2011.65>
- Roach, L. A., Bitz, C. M., Horvat, C., & Dean, S. M. (2019). Advances in modeling interactions between sea ice and ocean surface waves. *Journal of Advances in Modeling Earth Systems*, *11*(12), 4167–4181. <https://doi.org/10.1029/2019MS001836>
- Roach, L. A., Horvat, C., Dean, S. M., & Bitz, C. M. (2018). An emergent sea ice floe size distribution in a global coupled ocean–sea ice model. *Journal of Geophysical Research: Oceans*, *123*(6), 4322–4337. <https://doi.org/10.1029/2017JC013692>
- Rolph, R. J., Feltham, D. L., & Schröder, D. (2020). Changes of the Arctic marginal ice zone during the satellite era. *The Cryosphere*, *14*(6), 1971–1984. <https://doi.org/10.5194/tc-14-1971-2020>
- Rynders, S., Aksenov, Y., Feltham, D. L., Nurser, A. J. G., & Madec, G. (2022). Impact of granular behaviour of fragmented sea ice on marginal ice zone dynamics. In J. Tuhkuri & A. Polojärvi (Eds.), *IUTAM symposium on physics and mechanics of sea ice* (pp. 261–274). Springer International Publishing. https://doi.org/10.1007/978-3-030-80439-8_13
- Shaw, W. J., Stanton, T. P., McPhee, M. G., & Kikuchi, T. (2008). Estimates of surface roughness length in heterogeneous under-ice boundary layers. *Journal of Geophysical Research*, *113*(C8), C08030. <https://doi.org/10.1029/2007JC004550>
- Shen, H. H., Hibler, W. D., Lepparanta, M., & Leppäranta, M. (1987). The role of floe collisions in sea ice rheology. *Journal of Geophysical Research*, *92*(C7), 7085–7096. <https://doi.org/10.1029/JC092iC07p07085>
- Shrestha, K., & Manucharyan, G. E. (2021). Parameterization of submesoscale mixed layer restratification under sea ice. *Journal of Physical Oceanography*, *1*(3), 419–435. <https://doi.org/10.1175/JPO-D-21-0024.1>
- Smith, M., & Thomson, J. (2019). Ocean surface turbulence in newly formed marginal ice zones. *Journal of Geophysical Research: Oceans*, *124*(3), 1382–1398. <https://doi.org/10.1029/2018JC014405>
- Stern, H. L., Schweiger, A. J., Zhang, J., & Steele, M. (2018). On reconciling disparate studies of the sea-ice floe size distribution. *Elementa: Science of the Anthropocene*, *6*(1), 49. <https://doi.org/10.1525/elementa.304>
- Strong, C., & Rigor, I. G. (2013). Arctic marginal ice zone trending wider in summer and narrower in winter. *Geophysical Research Letters*, *40*(18), 4864–4868. <https://doi.org/10.1002/grl.50928>
- Timmermans, M.-L., Cole, S., & Toole, J. (2012). Horizontal density structure and restratification of the Arctic Ocean surface layer. *Journal of Physical Oceanography*, *42*(4), 659–668. <https://doi.org/10.1175/JPO-D-11-0125.1>
- Timmermans, M.-L., & Marshall, J. (2020). Understanding Arctic Ocean circulation: A review of ocean dynamics in a changing climate. *Journal of Geophysical Research: Oceans*, *125*(4), e2018JC014378. <https://doi.org/10.1029/2018JC014378>
- Tsamados, M., Feltham, D. L., Schroeder, D., Flocco, D., Farrell, S. L., Kurtz, N., et al. (2014). Impact of variable atmospheric and oceanic form drag on simulations of Arctic sea ice. *Journal of Physical Oceanography*, *44*(5), 1329–1353. <https://doi.org/10.1175/JPO-D-13-0215.1>
- Wang, Q., Marshall, J., Scott, J., Meneghello, G., Danilov, S., & Jung, T. (2019). On the feedback of ice–ocean stress coupling from geostrophic currents in an anticyclonic wind regime over the Beaufort Gyre. *Journal of Physical Oceanography*, *49*(2), 369–383. <https://doi.org/10.1175/JPO-D-18-0185.1>
- Wenta, M., & Herman, A. (2018). The influence of the spatial distribution of leads and ice floes on the atmospheric boundary layer over fragmented sea ice. *Annals of Glaciology*, *59*(76pt2), 213–230. <https://doi.org/10.1017/aog.2018.15>
- Wenta, M., & Herman, A. (2019). Area-averaged surface moisture flux over fragmented sea ice: Floe size distribution effects and the associated convection structure within the atmospheric boundary layer. *Atmosphere*, *10*(11), 654. <https://doi.org/10.3390/atmos10110654>
- Wu, Y., Wang, Z., & Liu, C. (2021). Impacts of changed ice-ocean stress on the North Atlantic ocean: Role of ocean surface currents. *Frontiers in Marine Science*, *8*, 628892. <https://doi.org/10.3389/fmars.2021.628892>